Optimization of Central Receiver Concentrated Solar Thermal: Site Selection, Heliostat Layout & Canting

by

Corey J. Noone

Submitted to the Department of Mechanical Engineering
in partial fulfillment of the requirements for the degree of

Master of Science in Mechanical Engineering

at the

MASSACHUSETTS INSTITUTE OF TECHNOLOGY

September 2011

Author .....
Department of Mechanical Engineering
August 5, 2011

Certified by...
.....
Alexander Mitsos
Rockwell International Assistant Professor
Thesis Supervisor

Accepted by.....
.....
David E. Hardt
Ralph E. and Eloise F. Cross Professor of Mechanical Engineering
Chairman, Department Committee on Graduate Theses

Optimization of Central Receiver Concentrated Solar Thermal: Site Selection, Heliostat Layout & Canting

by

Corey J. Noone

Submitted to the Department of Mechanical Engineering
on August 5, 2011, in partial fulfillment of the
requirements for the degree of
Master of Science in Mechanical Engineering

Abstract

In this thesis, two new models are introduced for the purposes of (i) locating sites in hillside terrain suitable for central receiver solar thermal plants and (ii) optimization of heliostat field layouts for any terrain. Additionally, optimization of heliostat canting, is presented as an application of the heliostat layout optimization model. Using the site selection model, suitable sites are located based on heliostat field efficiency and average annual insolation. By iteratively defining the receiver location and evaluating the corresponding site efficiency, by sampling elevation data points from within the defined heliostat field boundary, efficiency can be mapped as a function of the receiver location. The case studies presented illustrate the use of the tool for two field configurations, both with ground-level receivers. The heliostat layout optimization model includes a detailed calculation of the annual average optical efficiency accounting for projection losses, shading & blocking, aberration and atmospheric attenuation. The model is based on a discretization of the heliostats and can be viewed as ray tracing with a carefully selected distribution of rays. The prototype implementation is sufficiently fast to allow for field optimization. In addition, inspired by the spirals of the phyllotaxis disc pattern, a new biomimetic placement heuristic is described and evaluated which generates layouts of both higher efficiency and better ground coverage than radially staggered designs. Case studies demonstrate that the new pattern achieves a better trade-off between land area usage and efficiency, i.e., it can reduce the area requirement significantly for any desired efficiency. Finally, heliostat canting is considered. Traditionally, canting has been parabolic, in which the focal point of the heliostat lies on the axis of symmetry. Two alternative off-axis canting methods are compared in this thesis, fixed facet (static) canting in which the facet alignment is optimized for a single design day and time and then rigidly mounted to the frame and dynamic canting in which the facets are actively controlled such that the center of each facet is always perfectly focusing. For both methods, two case studies are considered, a power tower with planar heliostat field and a hillside heliostat field which directs light down to a ground-level salt pond.

Thesis Supervisor: Alexander Mitsos
Title: Rockwell International Assistant Professor

Acknowledgments

This thesis would not have been possible without the innumerable support of family, friends, and colleagues, past and present. I would like to specifically thank a few.

Foremost, I would like to express sincere gratitude to my advisor for his dedication to my work and well-being. Without his sacrifice of time and energy, my graduate experience would not have been nearly as rewarding.

To my dad, whose selfless devotion to his family drives me. To my mom, who has taught me that with an open heart and mind, drive finds purpose. To my brother, who I could not be more proud of, his intelligence and determination is a constant source of inspiration.

To my life long friends, for always giving me their support and confidence. I would not be the person I am today without them. In particular, I thank James Albrecht, though with us now in memory, for believing in me more than I did myself.

To my colleagues and coauthors, my publications are much richer for their contributions. Specifically, I thank Manuel Torrilhon for his suggestion of the spiral heliostat pattern inspired by the configuration of florets on the head of a sunflower. I would also like to thank Aris Bonanos for suggesting an analysis of heliostat canting and his expertise in our subsequent discussions.

Finally, I gratefully recognize funding from the Cyprus Research Promotion Founding for the Cyprus Institute MIT Alliance under account number 6918992.

Contents

List of Figures

List of Tables

Chapter 1

Site Selection for Hillside Central Receiver Solar Thermal Plants

1.1 Introduction

A simplified model utilizing digital elevation data is presented for the selection and evaluation of potential hillside sites for central receiver solar thermal plants. The primary intent of developing the model is for locating suitable sites for ground-level receivers, such as the so called CSPonD concept [30, 28, 29]. In the CSPonD design, the radiation concentrated by the heliostats is directly beamed down into a molten salt which serves as a combined receiver and thermal energy (exergy) storage medium. In addition to ground-level receivers, the model can also be used for receivers of any height and in any terrain. However, the advantages of utilizing ground-level receivers (made possible by hillsides) include the elimination of many significant costs and operating problems associated with tower systems, such as salt freezing in pipes, the capital cost and maintenance of high pressure pumps, and of course the capital cost of the tower. Additionally, terrain that is otherwise difficult to develop is suitable for hillside concentrated solar applications. As a result, hillside heliostat fields further decrease capital cost relative to traditional CSP sites because they do not require flat land, a resource of limited availability and high demand. A potential disadvantage of hillside sites is the increased cost of installing heliostats on hillside terrain.

One such example of using a hillside heliostat field is the world's largest solar furnace located at Odeillo, Font-Romeu in the French Pyrenees, consisting of 63 heliostats and having a nominal power rating of 1 MWt [11]. Despite the precedence of using hillsides, no tools exist in the open literature for locating sites suitable for hillside heliostat configurations nor predicting the efficiency and nominal power rating for non-planar sites, outside of ray-tracing software, motivating the development of the model described herein. While ray-tracing is an extremely useful tool and could be used for the evaluation of non-conventional heliostat fields, its most significant drawback is the required computation time. For instance, the case study of the western United States, as shown in Figure 1-7, required evaluating approximately 375 million candidate receiver locations. Therefore, the ability to scan vast areas to locate sites most suitable for CSP technologies necessitates a simplified model that does not require detailed calculations, which is why ray-tracing tools are not suitable for this purpose. The code most similar to the one proposed is the University of Houston's cellwise performance model. It calculates the annual site efficiency for cells, or representative points on the heliostat field, instead of on an individual heliostat basis [13].

With the use of digital elevation data, the model presented evaluates sites by calculating the average annual field efficiency of a set of sampled locations within the extent of the heliostat field boundary, the dimensions of which are defined as model parameters and are a function of the plant's nominal power. The sampled elevation data do not correspond to the heliostat positions in an optimal heliostat layout, but are used to approximate the efficiency of a heliostat field. Included in the calculation of field performance are (i) cosine efficiency, i.e., the ratio of the projected heliostat area in the direction of beam insolation to the surface area, (ii) shading and (iii) blocking losses due to nearby hillsides and other sampled locations. Two significant efficiency terms not included in this model are heliostat reflectivity and spillage. Excluding both is justified because they are primarily independent of the location of the heliostat field. Heliostat reflectivity is constant and spillage is predominately a function of distance from the receiver, which is a function of the

heliostat field size and is constant in the application of the model. As a result, the efficiencies reported are a product of a simplified model accounting for cosine, shading and blocking. With reasonable assumptions for reflectivity and spillage, the representative efficiency reported by the model could be adjusted to reflect the true efficiency of the site. The approach of a simplified model is justified by the ability to capture the most significant factors affecting heliostat field efficiency and is used to provide a list of candidate sites from a potentially very large region. The results of this model do not represent the final stage in site selection nor a substitute for a detailed calculation of field performance. Further, economic metrics such as the levelized cost of energy (LCOE) will ultimately be the determining factors in the technology, configuration, and the location used. While any region can be evaluated with this tool, the resolution of data sufficient for use in this model is currently only publicly available for certain regions of the world, for instance the USA. In order to accurately calculate the factors that affect heliostat field efficiency, the resolution of the elevation data used must be capable of capturing variations in terrain on the scale of heliostat separation distances.

Two receiver configurations are investigated in this article: beam-up, in which the receiver is located at a higher elevation than the heliostats, and beam-down, in which the receiver is located at a lower elevation than the heliostats. This terminology is not to be confused with the definition of beam-down commonly used in literature to describe a configuration in which a reflector is located on a tower to redirect energy downwards toward the receiver [37]. In this article, the terms "beam-up" and "beam-down" are used to describe the elevation of the receiver relative to the heliostat field. The case studies consider direct absorption pond receivers [30]. Therefore, a reflector is necessary in the beam-up configuration and is close to the receiver (e.g., not on top of a tower). The design of the pond is contingent on variables including the properties of the salt and the required storage capacity, and is beyond the scope of this article; however, the size of the receiver aperture is expected to be no larger than a traditional receiver because the heliostat fields are of comparable sizes. As a result, the model proposed and conclusions presented are primarily independent of the receiver type.

In the first case study, the area around White Sands, NM, two scenarios are investigated, (i) the beam-up site configuration with a secondary reflector having an optical efficiency of 0.9 used to direct the radiation into the pond, and (ii) the beam-down site configuration. Additional configurations are possible, such as a solar furnace as in Odeillo or replacing the pond in the beam-up configuration with a traditional receiver (without the need for a tower). In the case of a solar furnace, a concentrator may be used, however no distinction needs to be made between heliostats located at a higher elevation than the receiver and those lower than the receiver. This simply means removing the penalty of the concentrator's optical efficiency. Finally, the configuration of using a traditional receiver without a tower would be the same as in case (i) but without the loss incurred due to the secondary reflector, i.e., the efficiency of a site with a traditional receiver in a beam-up configuration is calculated as the beam-up pond configuration efficiency divided by 0.9. Neither of the final two configurations are considered in the case studies because they are simple modifications of the pond configuration.

The structure of the subsequent sections is as follows. Section 1.2 describes all major aspects of the model including the elevation data used for the case studies, the calculation of cosine losses as well as shading and blocking, the methodology for evaluating heliostat field performance, and lastly the post-processing required to visualize the results. Section 1.3 demonstrates the use of the model in case studies. Lastly, Sections 1.4 and 1.5 summarize the results from the application of the model as well as conclusions based on the different site configurations considered in this article.

For simplicity in the following, it is assumed that the sites considered are located north of the Tropic of Cancer, such that the sun is always to the south of the receiver at solar noon. Therefore, the corresponding heliostat field is most efficient north of the receiver. The tools and results presented in this article are expected to hold for sites to the south of the tropics with minimal changes to the model.

1.2 Model Description

The model proposed consists of designating candidate receiver locations on a grid of uniform spacing for a predefined region. At each iteration in which a receiver location is evaluated, the heliostat field is sampled by selecting points within the extent of the heliostat field boundary and using digital elevation data to determine the position relative to the receiver, from which the average annual efficiency is calculated for each location. Then, the total field efficiency corresponding with each receiver location is approximated as the average of the efficiencies from the sampled locations.

1.2.1 Elevation Data

The digital elevation data used in the analysis of US sites is publicly available as a result of a joint project by the United States Geological Survey (USGS), the National Aeronautics and Space Administration's (NASA) Jet Propulsion Laboratory (JPL), and the National Geospatial-Intelligence Agency (NGA). Specifically, the data set is from the Shuttle Radar Topography Mission (SRTM), with one arc-second resolution between elevation data points (SRTM1 v2.1 [32]), corresponding to roughly 30 meters on the horizontal plane. Due to the coarseness of the data, the analysis is based on a simplified model of approximating site efficiency. Data is also available from the same database for regions outside of the United States, but at a lower resolution of three arc-seconds per sample. This resolution corresponds to roughly 90 meters between samples, which is much larger than typical distances between heliostats, and is therefore of insufficient resolution to accurately capture variations in terrain at the scale necessary to evaluate a heliostat field.

Errors in the SRTM elevation data can be categorized based on the distances on the horizontal plane in which they occur. Measurement errors occurring over large distances do not significantly affect the results of this model because the magnitude of the error does not change much across the heliostat field. In contrast, random errors have much shorter correlation distances, approximately 100 meters or less, affecting the heliostat layout by varying the relative error of each sampled location with respect

to the receiver. However, most of the database has less than 5 meters random error in the z-direction [26], resulting in negligible angular variations for sampled locations at typical distances between heliostat and receiver. Therefore, neither cause of error significantly affects the results of the model. Factors not captured by elevation measurements such as land coverage (vegetation or human-made) and existence of bodies of water need to be accounted for prior to a final decision on site location.

1.2.2 Calculation of Average Annual Cosine Efficiency

Calculating the cosine efficiency for each sampled point during the site evaluation is in principle a computationally expensive process because it is time-dependent and requires time averaging. However, cosine efficiency is a function of position and is a smooth, well-behaved function of only three variables. Therefore, an efficient implementation is to generate a multi-dimensional table of cosine efficiency as a function of the discretized receiver azimuth and altitude angles, (see Figure A-1 for their definitions) [10], as well as the latitude of the site. The resolution of the variables is chosen such that the maximum error between two adjacent values in the table is less than one percent. Table 1.2.2 shows the range and resolution of each parameter used for tabulation.

Table 1.2.2 Cosine Efficiency Tabulation Parameters

	Range and Resolution [°]		
	Minimum	Maximum	Resolution
Azimuth	-180	180	1
Altitude	-90	90	1
Latitude	25	50	1

For each tabulated value, the average annual cosine efficiency is the irradiation-weighted mean of the instantaneous cosine efficiency integrated over a year, as shown in (1.1), where instantaneous beam radiation is calculated using version one of the Meteorological Radiation Model (MRM v1) for direct beam irradiance in clear sky

conditions [4].

$$\eta_{\text{cosine, year}} = \frac{\sum_{\text{day}=1}^{365} \int_{\text{sunrise}}^{\text{sunset}} \eta_{\text{cosine}}(t) q_{\text{beam}}(t) dt}{\sum_{\text{day}=1}^{365} \int_{\text{sunrise}}^{\text{sunset}} q_{\text{beam}}(t) dt} \tag{1.1}$$

The MRM calculates hourly beam irradiance at the earth's surface as a function of extraterrestrial solar irradiance and optical transmittances due to water vapor, mixed gases, ozone, and Mie and Rayleigh scattering. The clear sky model is used because it captures variations in insolation as a function of time without accounting for local weather conditions. The advantage of using this simplified radiation model is that cosine efficiency is easy to tabulate without the addition of local weather parameters. This is sufficient for use of the site selection model in small areas, such as the case study of White Sands, NM, because the variation in direct normal insolation is negligible, so the insolation weighting should be approximately the same. However, the assumption of clear sky conditions is not valid when considering large areas where variations in insolation can not be ignored. Therefore, in the case study of the western United States (Section 1.3.2), data from the National Solar Radiation Data Base [2] was additionally used to weight site efficiency in order to distinguish between sites having vastly different annual average direct normal insolation.

Figure 1-1(a) shows the dependence of yearly average cosine efficiency on the receiver azimuth and altitude angles with respect to a sampled heliostat field location at a constant latitude of 35°N (northern hemisphere). For the latitude selected, the maximum cosine efficiency occurs when the receiver is directly south of the heliostat and elevated roughly 60° from the horizontal plane. Figure 1-1(b) illustrates a subset of the data shown in Figure 1-1(a), having a constant receiver azimuth of 0°, showing the effect of varying the receiver altitude angle. For instance, the average annual cosine efficiency of a heliostat at 35°N latitude, and receiver located at 0° azimuth and 60° altitude, is 92%. Keeping everything else constant, a receiver at an altitude angle of −20° has a cosine efficiency of 75%, a difference of 17%. While comparing

two receiver altitude angles is not an accurate representation of an entire heliostat field, the difference in efficiencies of a field with a ground-level receiver versus an elevated receiver can be significant due to projection losses.

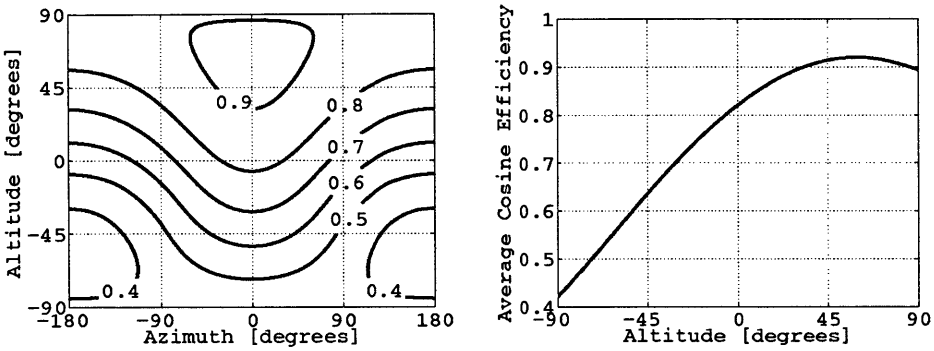

(a) Average Annual Cosine Efficiency as a Function of Receiver Azimuth and Altitude Angles at 35°N Latitude

(b) Average Annual Cosine Efficiency as a Function of Receiver Altitude Angle at 35°N Latitude and 0° Azimuth

Figure 1-1: Average Annual Cosine Efficiency as a Function of Receiver Position Relative to a Heliostat

1.2.3 Calculation of Shading by Southern Hillsides

Another factor of site evaluation is the potential shading of the heliostat field by southern hillsides. This occurs when the altitude angle of a hillside south of a heliostat is greater than the altitude angle of the sun at any time such that their azimuth angles are the same. This scenario poses a significant problem because locations which utilize hillside heliostat fields are likely to be in mountainous terrain, where there is a possibility that an adjacent hillside shades part or all of the heliostat field. However, checking a very large area in all directions south of each elevation data point is computationally expensive. Therefore, prior to cosine and blocking calculations, the area to the south of the heliostat field between the angles of $\pm 45°$ azimuth is checked for hillsides with an altitude angle greater than the minimum yearly solar altitude angle. The value of $\pm 45°$ is chosen because it represents a range in the solar state space which corresponds with peak daily insolation. This check is done once in increments of five degrees and 100 meters in a two kilometer radius for a single

representative location in the middle of the heliostat field. Recognizing that some amount of shading may be acceptable, this representative location is chosen to be at the center of the heliostat field. This way, while some shading may be acceptable, there will never be a case in which more than half of the heliostat field is ever shaded. This method is not a subsitute for a detailed calculation of shading, however is efficient due to the simplicity and ability to elminate sites in which nearby hillisides would clearly introduce too much shading for the site to be considered.

As for the implementation, the sun's minimum yearly altitude angle is tabulated as a function of two parameters, azimuth and latitude. If a southern hillside has an altitude angle greater than the minimum yearly solar altitude angle, the field will be approximately half shaded, or more, at least once a year. In this scenario, the corresponding receiver location is assigned an efficiency of zero and is excluded from further calculations. Computationally, this approach is extremely efficient compared to evaluating each individual heliostat and saves unnecessarily calculating the efficiency of a field that is significantly affected by shading. Figure 1-2 shows the result of tabulating the minimum yearly solar altitude angle for two latitudes, 25°N and 50°N, encompassing the contiguous United States. For example, a hill with an azimuth of 0° and an altitude angle of 25° will shade a heliostat located at 50°N latitude at least once per year, but never for a heliostat at 25°N latitude.

1.2.4 Site Selection Methodology

The methodology of selecting suitable hillside sites includes uniformly designating a receiver location and heliostat field boundary, sampling elevation data points from within the field boundary, and then calculating the yearly cosine efficiency while taking into account shading by earth and blocking. An exact calculation of shading and blocking between heliostats is not considered in this model because the sampled elevation data points do not represent an optimal heliostat layout. Instead, it is assumed that the effect of shading and blocking is small for an optimized heliostat layout and that cosine losses are a much larger factor in field efficiency; while shading and blocking may not be ignored, they need not be calculated in detail. In particular, it is

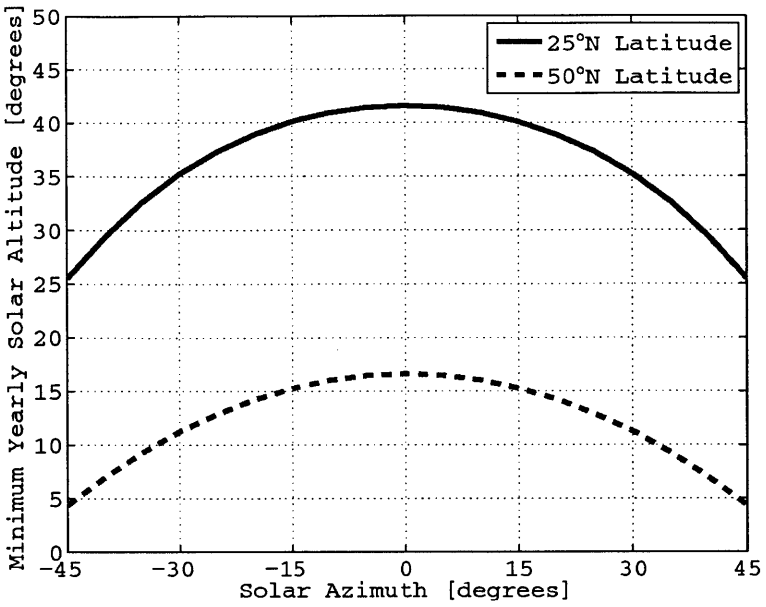

Figure 1-2: Minimum Yearly Solar Altitude vs Solar Azimuth

sufficient to determine whether a point on the heliostat field is blocked by comparing the receiver altitude angle for all sampled locations sharing the same azimuth angle and between the point and receiver. The following describes the process by which sites are evaluated.

The site evaluation methodology begins with designating a receiver location. Once the receiver is set, the heliostat field is defined by minimum and maximum azimuth angles as well as inner and outer radii (3D Euclidean distances), the area of which is a function of the total plant efficiency and nominal power. An example of a field with receiver azimuth angles between $\pm 45°$, and field radii between 150 and 500 meters, is shown in Figure 1-3 as projected on the horizontal plane. Each sampled field location is separated in increments of latitude and longitude corresponding with the resolution of the elevation data. The heliostat field is evaluated by referencing the tabulated cosine efficiency and checked for blocking at each location. The order in which points are selected is in increasing magnitude of the receiver azimuth angle for constant latitude, starting at the receiver, then progressively moving north. Therefore, successively sampled heliostat field locations have a radius greater than all other elevation data points having the same receiver azimuth angle. This ensures that all

heliostat field locations are evaluated in increasing radial distance in all directions and includes the land in between the receiver and the inner radius of the heliostat field. If the azimuth angle of the field location being evaluated has the same azimuth angle as any previously evaluated locations, the altitude angle of the current location must be less than the previous. Therefore, only the minimum altitude angle must be stored for any given azimuth direction. If the current altitude angle is greater than the minimum altitude angle recorded, the current field location is blocked and is assigned an efficiency of zero. If the current altitude angle is less than the minimum, then blocking does not occur and the efficiency of the location being evaluated is equal to the cosine efficiency. The total field efficiency is then calculated as the mean of all sampled heliostat field efficiencies. In Figure 1-3, a projection of the sampled locations on the horizontal plane is shown as an example, where the small squares are locations which experience blocking and therefore have efficiencies of zero, while every other point is shaded to represent the cosine efficiency of the corresponding location. Four of the five sampled locations shown as blocked are located in or near a small valley such that they have altitude angles greater than or equal to the altitude angles of the sampled points in between their positions and the receiver. Most importantly, these points are not meant to illustrate an actual heliostat layout nor the heliostat dimensions; instead, they are used to approximate the field efficiency based on the positions of the sampled points relative to the receiver and each other. A flow diagram illustrating the process of site selection is shown in Figure 1-4.

After all receiver locations are evaluated, the program writes the latitude, longitude, and efficiency of each location to file. The output is then analyzed with a geographic information system (GIS) software package, ArcMap v9.3 [9], and converted from vector data to a raster file, a method used for visualizing discrete data as a surface plot. For large areas, greater than 100 km^2, the raster file is created by a kernel density calculation which represents the efficiency per unit area within a defined radius specific to the scale of the image produced. Once an area of high efficiency is found, a more detailed raster file is created by interpolating the efficiencies of individual receiver locations to identify the exact optimal location for a receiver.

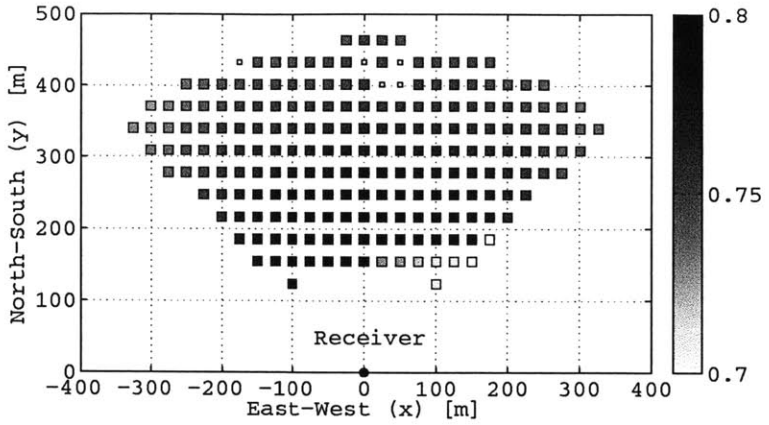

Figure 1-3: Example Illustrating Sampled Locations for Evaluating Site Efficiency
Icon shading indicates efficiency of individual sampled locations. Blocked locations are shown as small squares. This example field has a boundary defined by azimuth angles of $\pm 45°$ and radii of 150 and 500 meters.

The resulting raster data is then written to a KML file, an image overlay for viewing in Google Earth [15]. The image overlay drapes the terrain with a color map in which receiver efficiency is the scale, red representing high efficiency and blue as low efficiency.

1.3 Case Studies

Two case studies are presented. The first, White Sands, NM, is located in the southwest United States and was selected for its high average annual insolation. The area considered is roughly 10,000km^2 with pond receivers evaluated every 60 meters, resulting in approximately 2.8 million candidate receiver locations. The heliostat fields are defined by minimum and maximum azimuth angles of $\pm 45°$, and the minimum and maximum heliostat distance from receiver is 150 and 600 meters (area is approximately $265,000\text{m}^2$). The dimensions of the field roughly correspond with a 4MWe plant assuming the following: (i) a 30% heliostat surface area to land area ratio (i.e., coverage ratio), (ii) an average annual insolation of $250\frac{\text{W}}{\text{m}^2}$, (iii) a field efficiency of 60%, and (iv) a thermal to electric conversion efficiency of 35% (including the thermal efficency of the reciever, heat exchanger, and power cycle). The heliostat field is sampled every 30 meters, for approximately 200 samples per field. A second case study

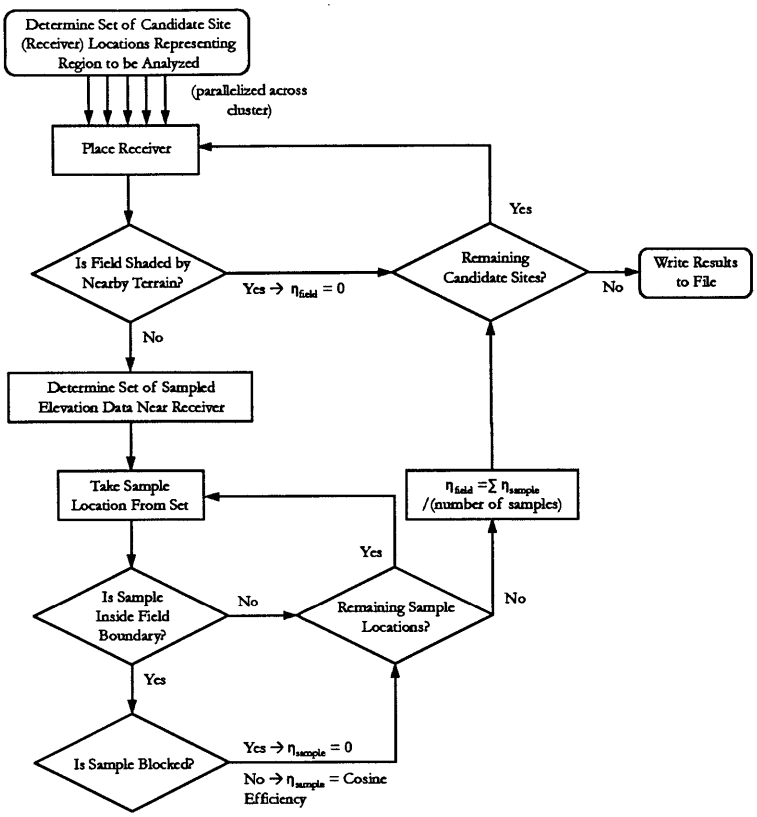

Figure 1-4: Flow Diagram Illustrating Site Selection Process

of the entire western United States is presented to illustrate the value of the model for large scale analyses and identification of regional variations in site efficiency.

In each case study, a single node on a Linux Intel Core 2 Quad Processor (2 GHz) PC with 8 GB memory was used. The first case study of White Sands, NM required approximately two hours to evaluate the 10,000km^2 area. The case study of the western United States required approximately 1000 CPU hours, scaling linearly with area from the White Sands, NM case study and was run on a cluster of four PCs utilizing eight nodes each as the model was parallelized using OpenMP.

1.3.1 White Sands, NM

The first case study, White Sands, NM, is located at 32.8°N latitude and 106.3°W longitude. The analysis is completed for two scenarios, (i) allowing a secondary reflector at the receiver with an optical efficiency of 0.9, and (ii) sites with a beam-

down configuration that do not require a secondary reflector. As stated in Section 1.1, the difference between these two scenarios is the reflector at the receiver, necessary for ponds located at a higher elevation than part or all of the heliostat field.

One of the highest efficiency sites from each of the field configurations considered are displayed in Figures 1-5 and 1-6. In these sites, the heliostat fields are shown north (right) of the receiver. The icons represent sampled elevation data locations used in the site efficiency calculation and not an actual heliostat layout, and the distances between the icons are larger than typical heliostat separation distances that would be seen in an actual field. The representative field efficiencies of the beam-up and beam-down sites are calculated to be 77% and 70%, respectively, a difference of 7% despite the 10% loss assumed for the secondary reflector. As stated in Section 1.1, these efficiencies are the result of a simplified model and do not include heliostat reflectivity and spillage losses. In any case, once found, candidate sites such as the ones shown would require a more detailed tool for heliostat placement and provide a more accurate calculation of field efficiency.

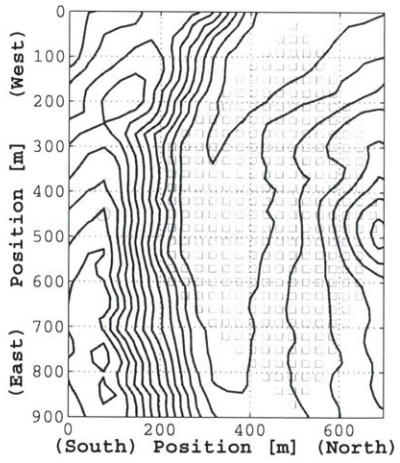

(a) Contour Plot of Elevation Data With 10m Contours

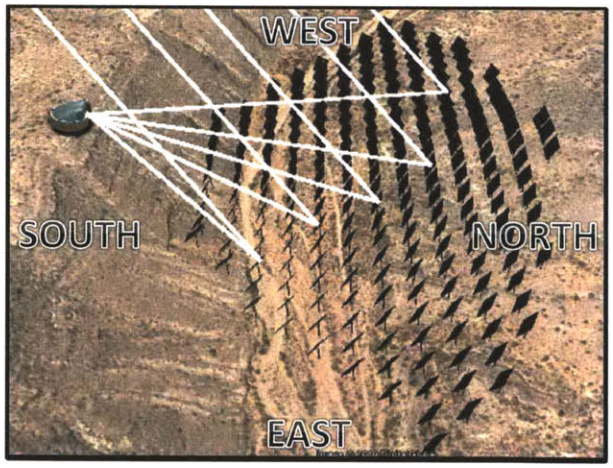

(b) West-Facing View of Site (In this site, the receiver is placed on top of a north-facing hillside and the heliostats are located on a relatively flat area of land north of the receiver.)

Figure 1-5: Potential Site for a Beam-Down Ground-Level Receiver in White Sands, NM (Icons denote receiver location and sampled locations from elevation data, not heliostat dimensions nor an actual heliostat layout.)

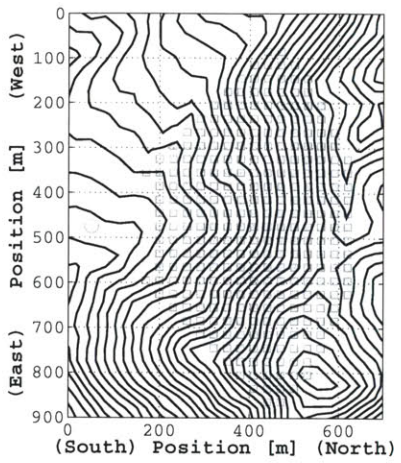

(a) Contour Plot of Elevation Data With 10m Contours

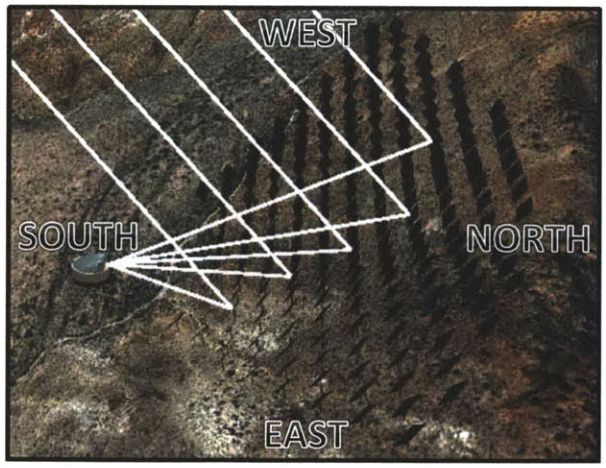

(b) West-Facing View of Site (In this site, the hillside heliostat field is south-facing and the receiver is located near the base of the hill.)

Figure 1-6: Potential Site for a Beam-Down Ground-Level Receiver in White Sands, NM (Icons denote receiver location and sampled locations from elevation data, not heliostat dimensions nor an actual heliostat layout.)

1.3.2 United States Ground-Level Receiver Site Potential

Figure 1-7 illustrates the result of applying the site selection model for the entire western United States, an area 500 times larger than the case study of White Sands. The purpose of this application of the model is to illustrate the regional variations in site potential. Most importantly, the availability of solar resources varies significantly by location. Therefore, instead of efficiency as the sole criterion, Figure 1-7 illustrates the product of efficiency and insolation, averaged using the kernel density method described in Section 1.2. Regions with the highest density of desirable sites are shaded dark (red), while regions with few or no suitable sites are light (yellow). This particular application of the model is for a heliostat field size corresponding to a 5 MWe power plant and a ground-level receiver for both beam-up and beam-down configurations, the same as the previous case study. Again, after the analysis for an area is complete, regional variations are easily identified and then either a more refined analysis or further post-processing can be done to identify the locations and efficiency of desirable sites for a particular heliostat field size and layout.

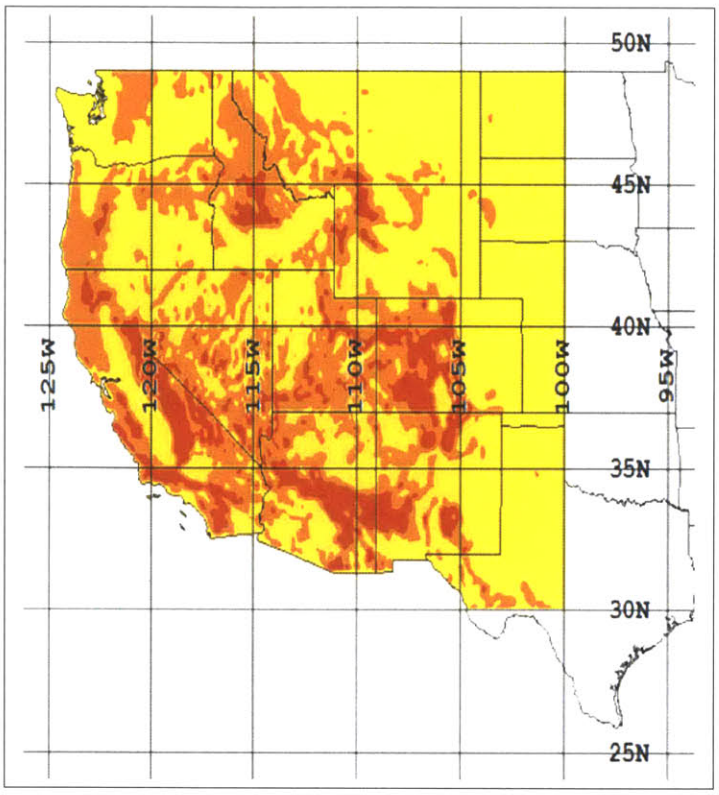

Figure 1-7: Western US Map Indicating Areas Most Suitable for Ground-Level Receiver Systems (Regions with high efficiency candidate sites are shaded dark (red) and low efficiency sites are light (yellow).)

1.4 Results

The following are the most significant results for selecting sites for ground-level central receiver applications. First is the heliostat field elevation compared to that of the receiver. In the highest efficiency receiver locations, the field is located at an elevation lower than the receiver, utilizing the terrain at the receiver as a natural tower. Despite accounting for a 10% loss associated with a secondary reflector herein (necessary for beam-up pond receivers), the difference between two optimal sites in the White Sands, NM case study is 7%. Returning to the simple example of heliostat position relative to receiver, located at the end of Section 1.2.2, and including a 10% loss to the efficiency of the heliostat field with an altitude angle of 60°, the difference in efficiencies is reduced from 17% to 8%. Therefore, the results from White Sands, NM case study match what was predicted in Section 1.2.2. Further, if a traditional receiver replaces

the pond in the beam-up configuration, the 7-8% difference relative to beam-down increases to approximately 17%. Nevertheless, while the simplified model is used to locate candidate sites suitable for solar thermal plants and is capable of evaluating a variety of heliostat field configurations and receiver types, economics merits such as the LCOE are the determining factors in the design and site selection process.

Further results of the analysis are locational trends. To illustrate why a beam-down receiver configuration would not be suitable for locations near the tropics, Figure 1-8 plots the effect of varying latitude on field cosine efficiency. In each plot, Figures 1-8(a) and 1-8(b), various heliostat locations are evaluated for a hillside of constant altitude angle relative to the receiver, with the average of these representative points plotted as the solid line. For field altitude angles of $-20°$ and $-30°$, the trend is an increasing field efficiency with increasing latitude. The caveat to the trend of increasing field efficiency with increasing latitude is the effect of shading, which is more prevalent with increasing latitude for areas of similar terrain. This is caused by the lower solar altitude angle, as shown in Figure 1-2, increasing the likelihood that a southern hillside will shade the heliostat field as well as increased shading by nearby heliostats. Another drawback of higher latitude locations is a lower average annual direct normal insolation. As a result, ideal candidate sites from case studies with both high efficiency and high insolation were found to be predominately in the southwest United States, where shading by heliostats is not a significant issue because of large solar altitude angles (sun high in the sky). Therefore, the calculation of shading by heliostats was omitted; however, if regions are considered with high insolation and high latitude, shading by heliostats should be addressed and a procedure similar to blocking could be implemented for a representative solar altitude (e.g., annual average) at discrete azimuth angle intervals.

1.5 Conclusions

Presented is a model and tool used for hillside central receiver site selection and evaluation. As a result of developing the model, the following conclusions are made. First,

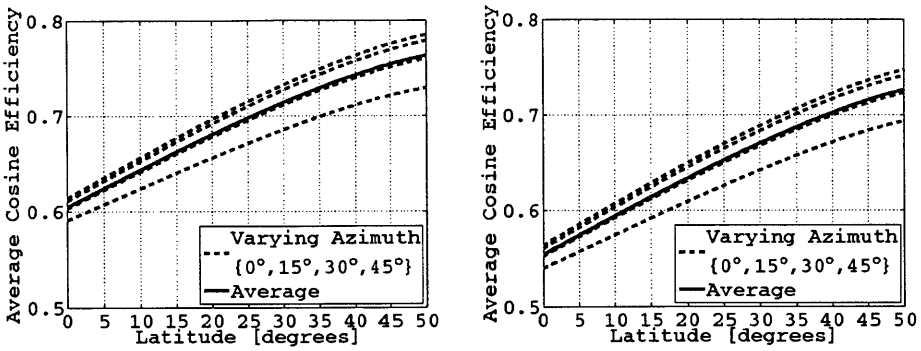

(a) −20° Altitude (b) −30° Altitude

Figure 1-8: Average Annual Cosine Efficiency vs Latitude (Decreasing Efficiency for Increasing Azimuth)

latitude and cosine efficiency are positively correlated for the beam-down configuration. When the pond is located at the ground level, the angle of incidence at the heliostat decreases with increasing latitude. Second, as a corollary to the previous result, due to a decrease in solar altitude angle with increasing latitude, the chance of shading by hillsides south of the heliostat field increases. Finally, the most advantageous receiver locations for ground-level receiver systems are elevated with respect to the heliostat field, utilizing the terrain at the receiver to create a natural tower.

The advantage of defining constant heliostat field dimensions for all evaluated sites is the computation time of the model. However, the drawback to this implementation is that the heliostat field dimensions are not optimal for all receiver locations. In other words, without calculating the optimal field dimensions for a given site, the evaluated site efficiencies are going to be a function of the model inputs. Therefore, caution must be used in the application of the model. One potential solution is to use a weighting factor to reflect the probability that a sampled location will be included in an optimized heliostat layout. For example, the perimeter of the heliostat field is more flexible than the center because a detailed tool is likely to calculate a heliostat layout in which the shape of the boundary is slightly different from the one predicted and used in this model, but the center of the field will surely be included. Using a weighting system to reflect uncertainty in the model parameters allows more flexibility

in the results.

The results of this model do not represent the final stage in site selection nor a substitute for a detailed calculation of field performance, which will be considered in future work.

Chapter 2

Heliostat Field Optimization: A New Computationally Efficient Model and Biomimetic Layout

2.1 Introduction

A new model is presented for the calculation of heliostat field optical efficiency, accounting for all significant factors affecting the performance of central receiver solar thermal systems including, (i) cosine losses, (ii) shading and blocking, (iii) receiver interception (i.e., heat not lost due to spillage), (iv) atmospheric attenuation between heliostat and receiver, and (v) heliostat reflectivity. The definition of each of these terms is common in the open literature [27] and a detailed description of their calculation in the model is presented in Section 2.2 (except for heliostat reflectivity which is assumed constant).

The purpose of developing this model, written in object-oriented Fortran 95, is for the gradient-based optimization of both traditional and non-traditional heliostat field layouts (e.g., on hillsides [21, 30]). This results in two main requirements, namely (i) computationally efficient calculation of efficiency with high accuracy and (ii) suitability for differentiation using AD tools [16, 17]. This article describes the new

model and proposes an improved biomimetic pattern for heliostat placement which substantially improves on the existing heuristics.

As a result of the intended purpose of optimization of heliostat field layouts, the proposed model was developed considering accuracy and computational efficiency, allowing for several distinguishing approaches to implementation. Firstly, Monte Carlo ray-tracing tools, such as SolTRACE [35], are accurate with a sufficient number of cast rays; however, the drawback is that they are computationally expensive for the purpose of evaluating instantaneous optical efficiency of large heliostat fields and are not a practical option for optimization of annual optical efficiency. SolTRACE is however used in Section 2.3 to validate the proposed model in small tests involving only the instantaneous heliostat field efficiency and the results of the two models show excellent agreement.

Secondly, the most expensive efficiency evaluation, that of shading and blocking, is calculated using a discretization of the heliostat surface. With a relatively coarse discretization, this method is both faster than exactly calculating the intersection exactly and is sufficiently accurate. Similar codes in the open literature assume that shading and blocking effects between multiple heliostats are distinct and therefore can be treated pairwise [20] (i.e., the shaded or blocked region of a heliostat is neither shaded nor blocked by another heliostat), or in an even more simplified case, that shading may be neglected and blocking assumed to be constant [8]. However, with a hierarchical approach to evaluating shading and blocking [5], these assumptions are not necessary at the heliostat level because the source of shading or blocking does not matter at the discretization level. In other words, the proposed model is similar to ray-tracing techniques in that whether a region shaded by one heliostat is also blocked by another heliostat is of no consequence because the ray does not reach its intended target in any scenario. If shading and blocking is calculated between heliostats pairwise, the resulting efficiency is either a lower or upper bound depending on whether the modeler assumes the pairwise effects are distinct or completely overlapping, respectively.

Thirdly, the receiver flux calculation is more accurate than assuming a single

error cone originating at the center of the heliostat, because the proposed model uses the surface normal at each discretization (or facet) to determine the direction of the reflected rays as a function of orientation on the heliostat. As a result, the effect of the time-variant optical error of aberration (i.e., astigmatism) is directly accounted for.

Finally, rather than iterating with a constant time step size, as is common practice in the open literature [20, 12, 36], the model presented takes steps in the solar state space. In the middle of the day when insolation is at peak and the solar azimuth changes the fastest (with respect to time), the proposed method takes small time steps relative to sunrise and sunset. This approach allows the model to retain the same accuracy as a constant time step implementation but requires much fewer iterations.

The structure of the subsequent sections is as follows. Section 2.2 describes all major aspects of the model, namely the calculation of solar position and insolation as well as each of the aforementioned efficiency factors presented in Equation (2.1). Section 2.3 validates the most computationally extensive components of the model (and thus most error-prone), specifically shading and blocking efficiency and interception efficiency. In terms of both implementation and computational expense, the much simpler evaluation of cosine, atmospheric attenuation, and reflectivity efficiencies are discussed in Section 2.2 and the implementations are validated with the open literature but do not warrant a detailed discussion. Section 2.4 demonstrates the application of the model by evaluating the design of the commercial scale power plant, PS10, as well as a new radially staggered configuration which performs better. Section 2.5 presents a new biomimetic spiral heuristic and is shown to outperform even the optimized radially staggered configuration. Lastly, Section 3.5 summarizes the model, applications, and heliostat placement heuristics presented.

2.2 Model Description

The instantaneous efficiency is calculated as the product of the instantaneous efficiency terms introduced in Section 3.1, where η_{cos} represents cosine (or projection)

losses, η_{sb} is shading and blocking, η_{itc} is the interception of heat at the aperture (i.e., heat not lost due to spillage), and η_{ref} is the heliostat reflectivity.

$$\eta = \eta_{cos} \cdot \eta_{sb} \cdot \eta_{itc} \cdot \eta_{\text{aa}} \cdot \eta_{\text{ref}}$$

Additionally, two average annual heliostat field efficiencies are calculated, the unweighted η_{year} and the insolation weighted $\eta_{\text{year,I}}$. The equation for the unweighted efficiency is identical to the insolation weighted efficiency with the exception that the insolation term $I_b(t)$ is removed.

$$\eta_{\text{year,I}} = \frac{\sum_{\text{day}=1}^{365} \int_{\text{sunrise}}^{\text{sunset}} I_b(t)\eta(t)dt}{\sum_{\text{day}=1}^{365} \int_{\text{sunrise}}^{\text{sunset}} I_b(t)dt}$$

2.2.1 Solar Position

In order to calculate the instantaneous heliostat field efficiency, as shown in Equation (2.1), a model for solar position is implemented. The solar positioning model [10] requires minimal computational expense, is sufficiently accurate, and has a simple functional form which is beneficial in the implementation of automatic differentiation tools used with gradient-based optimization algorithms. The solar declination, δ, and hour angle of sunrise and sunset as a function of day number, n_d, and latitude, ϕ (all angles in radians), are calculated as

$$\delta = \frac{23.45\pi}{180} \sin\left(2\pi \frac{284 + n_d}{365}\right)$$
$$\omega_{\text{sunrise}} = \cos^{-1}\left(\tan\phi \tan\delta\right) - \pi = -\omega_{\text{sunset}}$$

The sun's position relative to an observer on the ground is described by two angles,

the solar altitude and azimuth (Figure A-1).

$$\alpha = \sin^{-1}\left(\cos\phi\cos\delta\cos\omega + \sin\phi\sin\delta\right)$$
$$\gamma = \mathrm{sgn}\left(\omega\right)\left|\cos^{-1}\left(\frac{\sin\alpha\sin\phi - \sin\delta}{\cos\alpha\cos\phi}\right)\right|$$

While these equations are sufficiently accurate for heliostat placement, if more accurate solar positioning is required, models such as the Solar Position Algorithm (SPA) [24] are available.

2.2.2 Insolation

The model used for estimating hourly solar radiation is the first version of the Meteorological Radiation Model (MRMv1) [4], which accounts for several transmittance terms, but assumes cloudless skies. While this assumption prohibits the use of the model in much of the world, sites which are suitable for CSP rarely have extended periods of cloudy, overcast, or hazy weather. This model has been validated with measurements from select locations in the United States and southern European countries and has shown acceptable accuracy in capturing hourly, daily, and seasonal variations. While the MRM is used herein, countless alternate radiation models in the literature, and even measured data, can be used instead; insolation serves primarily as a weighting function.

2.2.3 Cosine Efficiency

The calculation of cosine efficiency is extremely simple using the Law of (specular) Reflection. The dot product of the directions of sun and heliostat (or facet) normal direction is related to the angle of incidence, θ_i.

$$\eta_{cos} = \cos\theta_i = \hat{\mathrm{d}}_{\mathrm{sun}} \cdot \hat{\mathrm{d}}_{\mathrm{n}}$$

For a paraboloid, the surface normal direction is calculated at any position by

differentiating the equation of the surface, where z is the normal direction of the center of the heliostat in the local coordinate system and f is the focal distance.

$$z - \frac{x^2 + y^2}{4f} = 0$$

$$\hat{\mathbf{d}}_n = \frac{1}{\sqrt{x^2 + y^2 + 4f^2}} \begin{bmatrix} -x \\ -y \\ 2f \end{bmatrix} \approx \begin{bmatrix} 0 \\ 0 \\ 1 \end{bmatrix} \qquad (\text{for } f \gg x, y)$$

2.2.4 Shading and Blocking Efficiency

An exact calculation of shading and blocking for a single heliostat, h_i, is accomplished by first calculating the pairwise intersection of h_i with every other heliostat in the directions of the sun and receiver, then finding the union of these intersections. Due to the computational expense, no existing code for heliostat field optimization calculates shading and blocking exactly; instead, either ray tracing techniques are used or assumptions are made about multiple interactions in order to eliminate the step of computing the union of shaded and blocked regions.

A sufficiently accurate and simple alternative is to use a discretization of h_i, as shown in Figure 2-1(a). The discretization points are projected in the directions of the sun and receiver for shading and blocking, respectively. If the projected point intersects the interior of another heliostat, the representative area on h_i is either shaded or blocked, while a point on the exterior is neither. For the purpose of increased accuracy (relative to only calculating whether or not intersection occurs), if the point is near the heliostat edge, a region of width equal to the discretization distance (δs as shown in Figure 2-1(b)), the amount of shading and blocking is interpolated as a function of distance from the edge. The interpolation method chosen can also be used to ensure that the model is differentiable, which may also be satisfied by time integration. The reason shading and blocking are combined into a single term is that in the implementation of the model, the shading and blocking efficiency of each discretization point is calculated as the minimum ratio of useful area to total area after projecting to each of

the other heliostats. For example, if the area represented by discretization point p is is partially shaded by h_i and partially blocked by h_j, the interaction which shades or blocks the largest area represents the efficiency of the discretized area. The shading and blocking of the entire heliostat is then calculated the mean efficiency of the set of discretization points. In terms of the implementation, the discretization points are calculated such that the separation distance in both the heliostat width and height is uniform. Recognizing that the effect of shading and blocking is typically small and thus confined to the edges, it would be advantageous to use a fine discretization near the heliostat edge and a coarse discretization in the middle; however, for the purpose of this article, only a uniform discretization is considered.

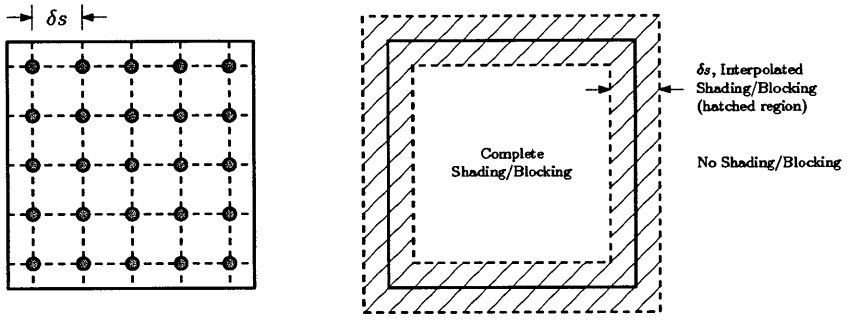

(a) Discretized Heliostat Surface

(b) Methodology for Calculation of Shading and Blocking of Projected Discretized Points

Figure 2-1: Schematic for Discretization Method of Shading and Blocking Calculation

The computational complexity of a pairwise comparison of heliostats can be reduced by only considering a subset of heliostats that can potentially shade or block heliostat h_i. This method, also referred to as the bounding sphere method [5], prevents unnecessary calculations for heliostats that are incapable of shading or blocking the heliostat currently being evaluated. Figure 2-2 illustrates how the method is used to determine whether h_2 is included in the subset of heliostats capable of potentially blocking heliostat h_1. If the distance d between the line segment connecting h_1 and the receiver (or the ray from h_1 in the direction of the sun) is less than the sum of the radii of the bounding spheres, r, then h_2 potentially blocks (or shades) h_1. By maintaining two lists of potentially shading and blocking heliostats for each h_i, the

complexity of the pairwise intersection calculation is reduced from $O(n^2)$ to $O(nm)$, where n is the total number of heliostats and m is the subset of heliostats evaluated for shading and blocking (typically $m \ll n$). Regardless of how shading and blocking is implemented, the much simpler calculation of the distance between a point and line segment significantly reduces the instances of the much more expensive calculation of shading and blocking. Additionally, while the subset of potentially shading heliostats needs to be updated for each time step due to the motion of the sun, the centers of the heliostats and receiver aperture are fixed with respect to time, so the subset of potentially blocking heliostats needs to be calculated only once.

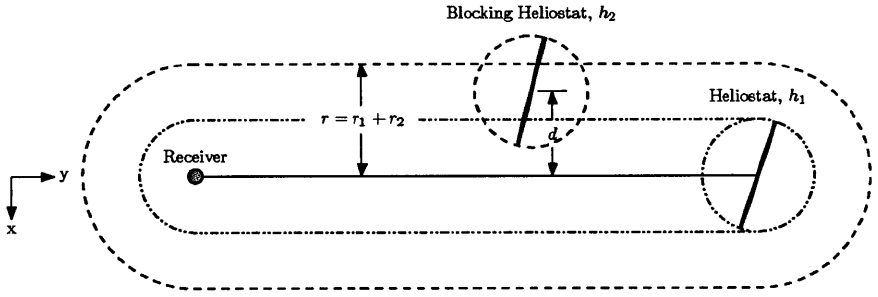

Figure 2-2: Schematic for Evaluation of Potential Blocking of Heliostat h_1 by Heliostat h_2

2.2.5 Interception Efficiency

The interception efficiency is calculated as a result of factors including off-axis aberration (i.e., astigmatism), surface errors such as microscopic imperfections and slope errors, tracking errors, and sun shape. The proposed model uses a similar discretization method as in the calculation of shading and blocking to determine the direction of the reflected rays at each point and the intersection of the reflected error cone with the plane of the aperture. The direction of the reflected ray as a function of direction of the sun (from the point of view of an observer) and the surface normal direction of the discretization (or facet) is calculated as

$$\hat{\mathbf{d}}_{\text{ref}} = 2\left(\hat{\mathbf{d}}_{\text{n}} \cdot \hat{\mathbf{d}}_{\text{sun}}\right)\hat{\mathbf{d}}_{\text{n}} - \hat{\mathbf{d}}_{\text{sun}}$$

Similar to existing codes [27, 13, 7, 36], the error cone of the reflected ray is approximated with flux density proportional to an angular Gaussian distribution [23]. The interception efficiency is then calculated as the integral of the power incident to the aperture divided by the total power incident to the plane of the aperture. As described in the following, the power incident to the plane of the aperture is the specular reflectance from the heliostats minus the atmospheric attenuation between heliostat and receiver. It is assumed in the model that each heliostat aims toward the center of the aperture. In reality, complex time-variant targeting strategies reduce the flux at the center of the aperture by (intentionally) spreading the incident radiation across the surface of the aperture. While these strategies mitigate the risk of dangerous flux levels at the center, the result is a lower interception efficiency. Therefore, the interception efficiency presented herein is an upper bound.

An advantage of using a discretization of the heliostat is that the curvature of the heliostat is accounted for when calculating the normal direction of each point during initialization of the heliostat field. Standard "on-axis" focusing or canting is modeled by fixing the focal point along the optical axis at a defined distance. The same procedure is used for asymmetric curvatures by defining a direction or solar position in which each heliostat is designed to focus. After the normal directions of the discretization points are defined, they too are rotated along with the position of the heliostat at each time step.

2.2.6 Atmospheric Attenuation Efficiency

Atmospheric attenuation accounts for radiation losses in the distance d_{rec} between a heliostat and the receiver and is calculated as

$$\eta_{aa} = \begin{cases} 0.99321 - 0.0001176 d_{\text{rec}} + 1.97 \cdot 10^{-8} d_{\text{rec}}^2 & d_{\text{rec}} \leq 1000\text{m} \\ \exp\left(-0.0001106 d_{\text{rec}}\right) & d_{\text{rec}} > 1000\text{m} \end{cases}$$

for d_{rec} in meters [27]. These losses are approximated assuming a visibility distance

of about 40 km. Similar equations exist in the open literature for varying visibilities [18, 20], but the difference is less than 1% in the range of visibilities typical of a clear day.

2.3 Model Validation

The most computationally extensive components of the model (and thus most error-prone), described in Section 2.2, specifically the terms shading and blocking efficiency and interception efficiency, are validated using the ray-tracing tool SolTRACE [35]. Additionally, the dependence of efficiency on discretization size and time step size are also investigated.

The model is validated with SolTRACE for several test cases shown below as well as the full heliostat fields shown in Section 2.4. In all of the cases, using a heliostat discretization of only 9 points (25 discretization points shown in Figure 2-1(a)), the error in shading and blocking efficiency is less than 10^{-3}. While this error is sufficiently small for heliostat placement, the error reduces to less than 10^{-4} using a grid of 100 points. Therefore, the method presented is both highly accurate even with a relatively coarse discretization.

Table 2.1: Interception Efficiency Validation Parameters

Location and Time	
Latitude	37°26' N
Day	March 20
Hour	3pm
Configuration	
Receiver Position (x,y,z)	$(0, 0, 115)$m
Receiver Normal Direction	$(0, 0.9763, -0.2165)$
Heliostat Position	$(300, 150, 5)$m
Heliostat Width	12.84m
Heliostat Height	9.45m

Interception efficiency was also validated using SolTRACE by first checking that the image of the concentrated light on the receiver (i.e., spot size) is consistent between the two programs. Shown in Figure 2-3(a) is the image produced by a single heliostat

at the configuration shown in Table 2.1 and assuming an ideal paraboloidal geometry (i.e., no facets or optical errors). Figure 2-3(b) is the image produced by SolTRACE, which show excellent agreement. Furthermore, an advantage of the implementation is that the time-dependent effects of off-axis aberration are directly accounted for by using a discretization of the heliostat.

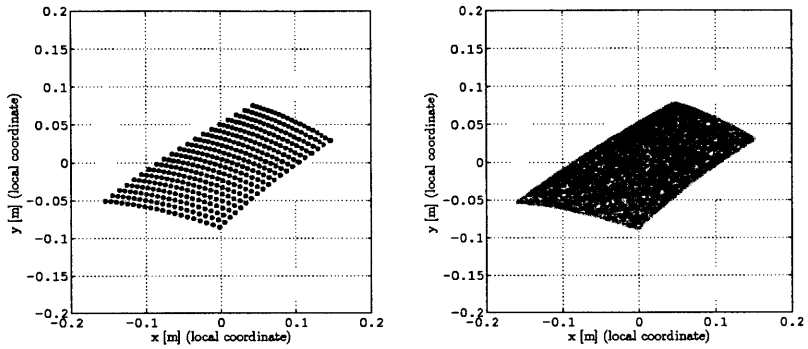

(a) Single Heliostat Spot Size Using Presented Model of Heliostat Discretization

(b) Single Heliostat Spot Size using SolTRACE (ray tracing)

Figure 2-3: Validation of Spot Size (neglecting optical errors) Shown in the Local Coordinates of the Receiver Aperture of a Single Heliostat

Based on the location of the discretization points and the direction of the reflected rays, the intersection of the rays with the receiver is known (Figure 2-3(a)). Then, the calculation of interception efficiency simply combines the optical errors, sun size, and the finite size of the facets into a representative error cone and an integration of the intersection of the error cone with the surface of the receiver. The resulting flux map from Figure 2-3 is shown in Figure 2-4, which was validated in SolTRACE by modeling the individual heliostat facets. Again, after including optical errors, the spot size and intensity show excellent agreement.

2.4 PS10 Validation and Redesign

PS10, the 11MWe power tower plant located in Andalusia, Spain [1, 3], is analyzed with the presented model for additional validation and benchmarking purposes. As detailed in Table 2.2, the heliostat field consists of 624 heliostats, each roughly 120m^2,

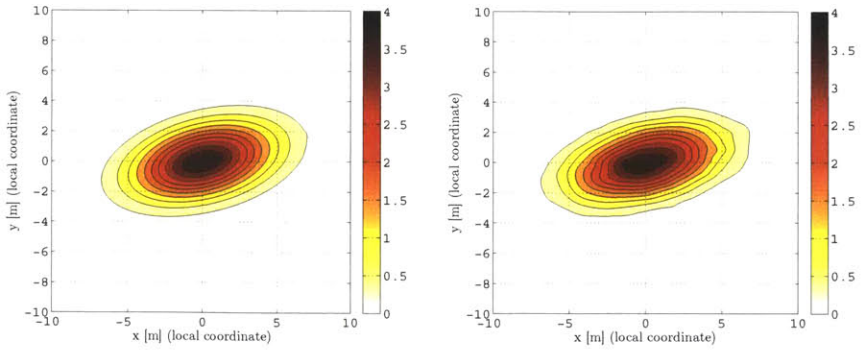

(a) Single Heliostat Spot Size using Presented Model

(b) Single Heliostat Spot Size using SolTRACE

Figure 2-4: Validation of Spot Size (including optical errors) using SolTRACE

arranged in a radially staggered configuration north of the 115m receiver tower. For the purposes of this analysis, the heliostat configuration is assumed to be planar despite the small variation in elevation of the PS10 site, with a maximum difference in elevation across the field of approximately 10 meters [1].

The first test case is the existing PS10 layout, generated by the Sandia code WinDELSOL1.0 [20, 34], shown in Figure 2-5(a). The resulting annual unweighted efficiency is 64%, the same value provided by Abengoa Solar [1] as well as results from previous modeling efforts [34]. Table 2.3 details a breakdown of the individual efficiency factors described in Section 2.2.

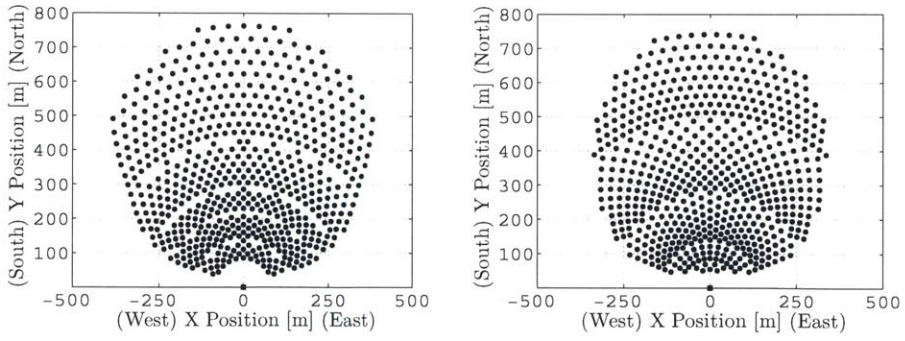

(a) Original PS10 Heliostat Field Configuration

(b) Redesigned PS10 Heliostat Field Configuration

Figure 2-5: Comparison of the Original PS10 Configuration with the Redesigned Configuration

Without changing any aspect of the plant other than heliostat positions, the layout

Table 2.2: PS10 Heliostat Field Parameters [1, 3]

Location	
Latitude	37°26' N
Longitude	6°15' W
Heliostats	(Sanlúcar 120)
Count	624
Width	12.84m
Height	9.45m
Reflectivity	0.88
$\sigma^2_{\text{optical}}$	2.9mrad
$\sigma^2_{\text{sun shape}}$	2.51mrad
Receiver	
Tower Height	115m
Normal Direction	$(0, 0.9763, -0.2165)$
Aperture Width	13.78m
Aperture Height	12m
Solar Model	
Distribution of Aerosol Particles, α	1.3
Turbidity Coefficient, β	0.1

of PS10 was redesigned using the presented model with a similar radially staggered heliostat placement heuristic described in Section 3.2. The new layout, shown in Figure 2-5(b) increases the optical efficiency $\eta_{\text{year,I}}$ by 0.19 percentage points and decreases the land area by about 10.9% (where land area is defined as the area of the convex hull of the (x, y) positions of the tower and heliostats), while maintaining the constraint that nearby heliostats must be separated by a minimum distance such that collision is not possible. Table 2.3 lists the individual efficiency factors. While the effect of atmospheric attenuation is greater in the improved radially staggered layout due to an increase in average distance from heliostat to receiver, interception efficiency is slightly improved by placing the heliostats closer to the normal direction of the receiver aperture so the intersection of the error cone with the aperture produces a smaller spot size. Most notably however, is that by placing the heliostats closer together, the total area of the field can be reduced significantly without sacrificing efficiency simply by trading a lower shading and blocking efficiency for a higher cosine efficiency.

2.4.1 Methodology of Heliostat Field Optimization

The heliostat field layout in Figure 2-5(b) was chosen by optimizing two parameters of the pattern which control the increase in distance between successive rows and when the rows split (i.e., when the distance between heliostats in a row is large enough that the angular separation between heliostats in the successive row can be split in half without the potential for heliostat collision or causing significant shading or blocking). The nominal values for radial and azimuthal (angular) spacing are from the DELSOL user's manual [20], where θ_L is the receiver aperture altitude angle with respect to a position on the ground (function of row radius), HM is the heliostat height, WM is the heliostat width, and THT is the tower height. The radial spacing has been divided by two from the original form of the equation to represent distance between successive rows.

$$\Delta r = \frac{1}{2}\left(1.14424\cot\theta_L - 1.0935 + 3.0684\theta_L - 1.1256\theta_L^2\right)\mathrm{HM}$$

$$\Delta az = \left(1.7491 + 0.6396\theta_L + \frac{0.02873}{\theta_L - 0.04902}\right)\mathrm{WM}\frac{2r}{2r - \mathrm{HM}\cdot\Delta r}\left(1 - \frac{\mathrm{HM}\cdot\Delta r}{2r\cdot\mathrm{THT}}\right)^{-1}$$

In the implementation of the model, a multiplier is added to the Δr term to modify the radial growth. Additionally, another parameter is used to control the azimuthal spacing (when the row splits) and is defined by the ratio of the angular separation of the current row and the Δaz term above. When this ratio exceeds the parameter value, the angular spacing of the row is halved from the previous row. This parameter optimization requires a computationally efficient model and is the primary reason why traditional ray-tracing tools were not used.

Specifically, the individual locations of the heliostats are determined by generating a pattern much larger than the expected size of the actual heliostat field using a known heuristic (e.g., the radially staggered pattern) and selecting parameter values (in this case, there are two) which control how large the pattern is and/or how quickly it grows. Next, all of these candidate locations are evaluated in the absence of shading

and blocking in order to quickly calculate efficiency neglecting interaction between heliostats. These candidate locations are then sorted by their individual efficiencies and the n heliostats with the highest efficiency are chosen to comprise the field. Finally, this field is then evaluated with all of the efficiency factors (including shading and blocking) to calculate the average annual insolation weighted efficiency of the entire field.

This process of generating the over-sized candidate set of heliostats, evaluating the set, and then selecting a prescribed number of heliostats is repeated for a finite set of parameter combinations in order to maximize the objective $\eta_{\text{year,I}}$ (as done for the improved radially staggered and phyllotaxis patterns, Figures 2-5(b) and 2-6(a), respectively). In the phyllotaxis pattern described in Section 2.5, the parameters optimized are a and b of Equation (2.2).

2.5 Biomimetic Heuristic

For tower receivers, the efficiency of an individual heliostat is typically higher near the tower than far away, see also Figures 2-7(a) and 2-8(a). Therefore, it seems preferable to have a higher density of heliostats near the tower than far away even at the expense of increased shading and blocking. The disadvantage of the radially staggered configuration is that the transition from high to low density is not continuous (unlike efficiency). Therefore, a new heuristic is presented, inspired from spiral patterns of the phyllotaxis disc, which has the advantage of a continuous density function. An example is the configuration of florets on the head of a sunflower [33], taking the form of Equations (2.1) and (2.2), where θ_k is linearly proportional to the k^{th} element of the sequence and r_k is the radial growth function, expressed by the constant exponentiation of k^{th} element. The angular component is related to the golden ratio φ, which equals $\frac{1+\sqrt{5}}{2}$. In the example of sunflowers, the coefficient b in the radial component equals 0.5, resulting in the form of Equation (2.2) known as Fermat's spiral. However, when b is 0.5, the mean distance between neighboring florets in the sunflower model is constant [19, 25]. In heliostat fields, it is beneficial to vary the heliostat pattern

density as a function of distance from the receiver, which is accomplished by allowing b to vary.

$$\theta_k = 2\pi\varphi^{-2}k \tag{2.1}$$

$$r_k = ak^b \tag{2.2}$$

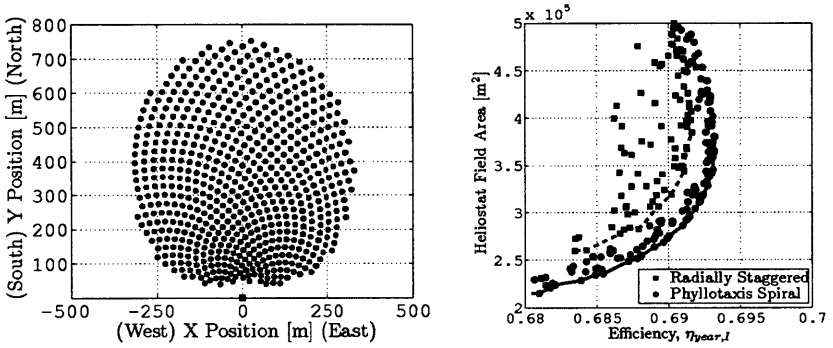

(a) Redesigned PS10 Heliostat Field Configuration Using the Phyllotaxis Spiral Heuristic

(b) Trade-off Between Heliostat Field Area and Field Efficiency

Figure 2-6: Redesigned PS10 Plant and Pareto Curves for Optimization of Heliostat Field Area and Efficiency

Applying the spiral pattern to heliostat placement yields the result shown in Figure 2-6(a). The values of the coefficients a and b are 4.5 and 0.65, respectively, and are obtained with the same approach of parameter optimization as the radially staggered results presented in Section 3.2, optimizing the heliostat field layout for combinations of a and b in the ranges of [2,8] and [0.5,0.7], respectively. Figure 2-6(b) illustrates the Pareto curve as it represents the trade-offs between the size of the heliostat field and efficiency across the range of parameters selected for both the radially staggered and phyllotaxis spiral patterns. In addition to the parameters shown, the center of the spiral pattern was varied along the north-south direction with respect to the tower; however, optimal field configurations resulted when the spiral pattern is centered at the receiver tower. The value of φ is not optimized because even small variations from the nominal $\frac{1+\sqrt{5}}{2}$ produces dramatically different patterns which were significantly

suboptimal. While other radial growth functions are considered, namely the logarithmic and Archimedean spirals, neither perform better than the growth function of Equation (2.2). This is due to the fact that the exponential and linear radial growth functions of the two spiral patterns below results in a much faster change in heliostat field density than Equation (2.2). As a result, either heliostats near the tower are placed too close together or heliostats far from the receiver are spread too far apart.

$$r_k = a \exp(b\theta_k) \qquad \text{logarithmic spiral}$$

$$r_k = a\theta_k \qquad \text{Archimedean spiral}$$

As detailed in Table 2.3, the spiral pattern significantly outperforms the radially staggered pattern. Compared to the design of PS10, the spiral pattern has an efficiency $\eta_{\text{year,I}}$ 0.36 percentage points higher while simultaneously reducing the size of the heliostat field by 15.8%.

Table 2.3: PS10: Breakdown of Heliostat Field Efficiency Terms and Heliostat Field Area

	radially staggered, WinDELSOL1.0 (Figure 2-5(a))	radially staggered, MIT (Figure 2-5(b))	phyllotaxis spiral, MIT (Figure 2-6(a))
	Unweighted Heliostat Field Efficiency		
η_{cos}	0.8283	0.8308	0.8310
η_{sb}	0.9255	0.9232	0.9264
η_{itc}	0.9926	0.9937	0.9938
η_{aa}	0.9498	0.9496	0.9491
η_{ref}	0.8800	0.8800	0.8800
η_{year}	0.6401	0.6409	0.6430
	Insolation Weighted Heliostat Field Efficiency		
$\eta_{\text{year, I}}$	0.6897	0.6916	0.6933
	Heliostat Field Area		
Area [x10^3m^2]	439	391	379

An advantage of the spiral pattern is that the density of heliostats better matches the pattern of heliostat efficiency as a function of position. Simply, the efficiency of the heliostat field is improved by placing more heliostats in a higher efficiency location

of the field until of course the effect of shading and blocking exceeds the incremental benefit in the remaining efficiency terms, which is the reason the coefficient b in Equation (2.2) required optimization instead of assuming the same value as for sunflowers. Figure 2-7(a) shows the layout of the redesigned PS10 plant with the radially staggered configuration. The color map indicates the efficiency of each heliostat position neglecting shading and blocking (used in the methodology for selecting the heliostat layout, as described in Section 2.4). Figure 2-7(b) represents the density of the heliostat field as a function of position by plotting the distance between neighboring heliostats as a function of position. Inherent in the radially staggered configuration is a non-monotonic heliostat density as a function of distance from the receiver. This is clearly suboptimal because the heliostats at the high density regions are incurring significant shading and blocking while the heliostats in the low density regions are not fully utilizing the high efficiency field positions. On the other hand, in the spiral pattern shown in Figure 2-8, the density function is both continuous and monotonic.

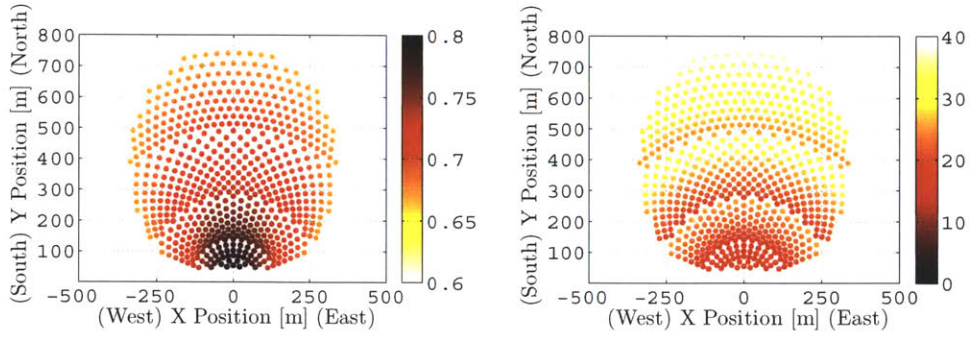

(a) Individual Heliostat Efficiency as a Function of Position (neglecting shading and blocking)

(b) Distance Between Neighboring Heliostats as a Function of Position

Figure 2-7: Comparison of Heliostat Efficiency and Density for the Improved Radially Staggered Configuration

Another benefit of the phyllotaxis spiral is that the polar angle of the heliostat locations, shown in Equation (2.1), is related to the irrational golden ratio φ. Therefore, no two heliostat centers share the same azimuth angle with respect to the receiver tower, as opposed to the radially staggered pattern, where every other row shares the same azimuth angle for every heliostat. Therefore, when blocking does occur in the

spiral pattern, it is more likely to be localized.

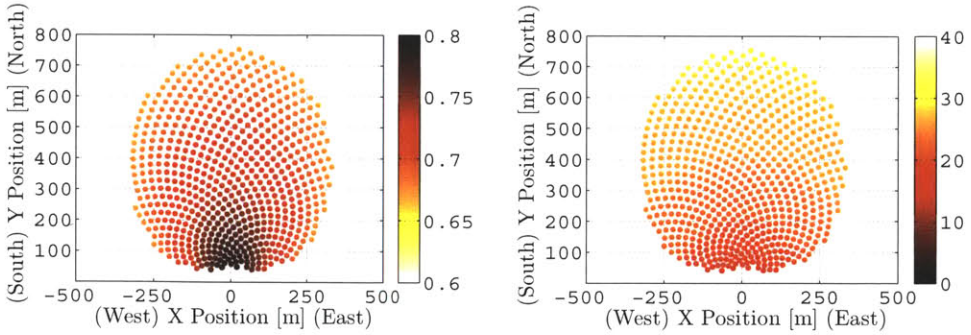

(a) Individual Heliostat Efficiency as a Function of Position (neglecting shading and blocking)

(b) Distance Between Neighboring Heliostats as a Function of Position

Figure 2-8: Comparison of Heliostat Efficiency and Density for the Phyllotaxis Spiral Configuration

Lastly, Table 2.4 presents the results of scaling the size of the field of PS10 to observe trends in efficiency and heliostat field area for larger plant sizes. At each heliostat field size, the parameters of the PS10 plant remain constant, except for the number of heliostats and size of the receiver aperture dimensions. The following function roughly calculates the diameter of the receiver aperture necessary to maintain the same interception efficiency as in PS10 for the optimized heliostat field as a function of the number of heliostats. This function is simply a polynomial fit of the annual average spot size at each of the field sizes and used to prevent high spillage losses, not the result of a detailed analysis in receiver design.

$$d_a = -2.42 \cdot 10^{-7} n_h^2 + 5.37 \cdot 10^{-3} n_h + 8.95$$

As the number of heliostats is increased from the original 624, the difference in field efficiency between the optimized phyllotaxis spiral pattern and the radially staggered pattern grows while maintaining a roughly 18% reduction in heliostat field area. In other words, the proposed pattern outperforms the radially staggered pattern and the difference between the two is more pronounced at larger field sizes.

Table 2.4: Field Efficiency Improvement and Land Area Reduction of the Optimized Phyllotaxis Spiral Relative to the Optimized Radially Staggered Pattern at Various Plant Sizes

Number of Heliostats	Percentage Point Improvement in Efficiency, $\eta_{\text{year,I}}$ [pp]	Percent Reduction in Land Area [%]
1000	0.1979	18.1
2000	0.3366	18.7
3000	0.3558	18.5

2.6 Conclusion

In this article, both a model and heuristic for heliostat field optimization are presented. The model, developed in object-oriented Fortran 95, is detailed herein and validated with the use of SolTRACE [35]. As presented in Section 3.1, the development of the model offers opportunities to improve upon existing methods for calculating heliostat field efficiency including a heliostat discretization approach which is both fast and accurate in the calculation of shading and blocking and spillage. Additionally the model takes iterations throughout the day in steps of solar state which results in more instantaneous field efficiency evaluations around solar noon when the rate of change of solar azimuth is fastest and when insolation is greatest, thus producing a more accurate integration with fewer iterations.

The PS10 power tower plant in Andalusia, Spain, is used as a demonstrative application which both shows results similar to those available in the open literature [1, 34] and the ability of the model to improve upon existing configurations. As shown in Section 2.4, even with the existing heuristic of placing the heliostats in radially staggered pattern, the optical efficiency of the heliostat field can be improved by 0.19 percentage points while simultaneously reducing the land area by 10.9% simply by optimizing the parameters of the heuristic.

Finally, a new heuristic inspired by disc phyllotaxis [33] is presented. Section 2.5 demonstrates the application of the spiral pattern by again redesigning the original heliostat field layout of PS10 for an improvement in optical efficiency of 0.36 percentage points and reduction in land area of 15.8%. Figures 2-7 and 2-8 illustrate the difference in radially staggered and spiral patterns' heliostat density and the ability to

utilize high efficiency land area. While the spiral pattern performs better than traditional approaches, there is likely still room for significant improvement by considering other functional forms and heuristics.

As mentioned in Section 3.1, future work includes the optimization of unconventional sites for heliostat fields, such as hillsides in the CSPonD concept [21, 30]. Without the simplifications used in planar layouts, hillsides are expected to rely more heavily on local optimization of individual heliostats and will require the automatic differentiation tools introduced with optimization algorithms to generate suitable heliostat configurations.

Chapter 3

Reduction in Spot Size via Off-Axis Static and Dynamic Heliostat Canting

3.1 Introduction

While central receiver plants are idealized as point concentrating systems, in actuality, the reflected power from a heliostat creates a finite size image on the receiver. This is obviously advantageous to avoid excessively high flux levels, but also means increased receiver sizes. Simply, by reducing the image size (or spot size) of each heliostat, the receiver can be made smaller and targeting strategies can more evenly distribute the incident power from all heliostats. Traditional parabolic canting provides ideal focusing when the heliostat, receiver, and sun are aligned, and thus he focal point lies in the line of symmetry of the paraboloid. However, for most heliostats in a typical field, the receiver is far from the axis of symmetry during periods of peak insolation, which results in significant aberration. In this article, two alternative canting methods are evaluated based on their average reduction in spot size. The reader is referred to [6] for a more detailed discussion and thorough literature review.

The structure of the article is as follows. Section 3.2 describes the methodology

used for defining the orientation of the facets and how canting performance is evaluated. Section 3.3 presents a case study based on [6] as a means of validating the approach described in Section 3.2. Finally, Section 3.4 presents the results of two case studies, namely a traditional planar heliostat layout with a tower receiver and a heliostat field located on a hillside which direct lights down to a ground-level salt pond. Both static and dynamic canting are considered. Lastly, Section 3.5 summarizes the results of the case studies.

3.2 Methodology

The approach used in this analysis for optimizing heliostat canting is to select a facet orientation which maximizes the power incident to the receiver (i.e., the interception efficiency). However, this requires assumptions on the receiver design (e.g., one or multiple flat/cavity apertures, external cylindrical receiver, etc.) and dimensions. Herein, an alternative metric that does not require assumptions on the receiver utilized is the average annual insolation-weighted spot size (or image) on a plane at the receiver and aligned normal to the incident power. Simply, if the receiver is flat and pointed directly at an individual heliostat, the spot size is the effective diameter determined to capture 98% of the incident power. Minimizing this spot size allows for smaller receiver sizes, higher interception efficiencies, and more complex targeting strategies geared toward uniform flux distribution at the receiver.

In the case studies presented, optimal canting at a single point in time is determined by aligning each facet such that the reflected ray from the facet center strikes the center of the receiver. While aberration is instantaneously eliminated, the spot size is not zero due to additional optical errors such as macroscopic and microscopic imperfections of the heliostat surface, sun shape (i.e., the sun is not a finite source), and in the case of non-focusing facets, the size of an individual facet. The model validation performed in Section 3.3 uses focused facets while the case studies in Section 3.4 use heliostats with flat facets.

In the case of *static* off-axis canting, the facet orientation is prescribed by a design

day and time, then fixed (relative to the common frame) and evaluated by calculating the average annual insolation-weighted spot size. This process is repeated for the entire year to determine the optimal day and time of day which results in a minimum spot size. In *dynamic* canting, the heliostat facets are assumed to be controlled such that at all time, the center of the facets are perfectly focusing. The results for both canting types are presented as the percent reduction in spot size compared to parabolic canting.

3.3 Model Validation

The model used herein for the calculation of heliostat spot size is an in-house model developed for heliostat field optimization (Noone et al. [22]) and has been validated using SolTrace [35]. However in [22], only on-axis parabolic canting is considered. In order to validate an application of off-axis canting, a case study from Buck and Teufel [6] is considered. In short, the average annual insolation-weighted interception efficiency is calculated for a single heliostat with off-axis canting as a function of design day and time, i.e., the point in time for which the heliostat is canted such that the center of each facet focuses perfectly on the center of the receiver aperture (zero aberration). In consistency with [6], the interception efficiency for a given receiver, as opposed to the proposed spot size metric, is considered. All parameters used (receiver design, facet size, heliostat location, etc.) are the same as in [6]. In Figure 3-1 the results of the in-house code are compared to the literature results and show excellent agreement in terms of efficiency magnitude, trends, extrema, and optimal design day and time that maximizes interception efficiency.

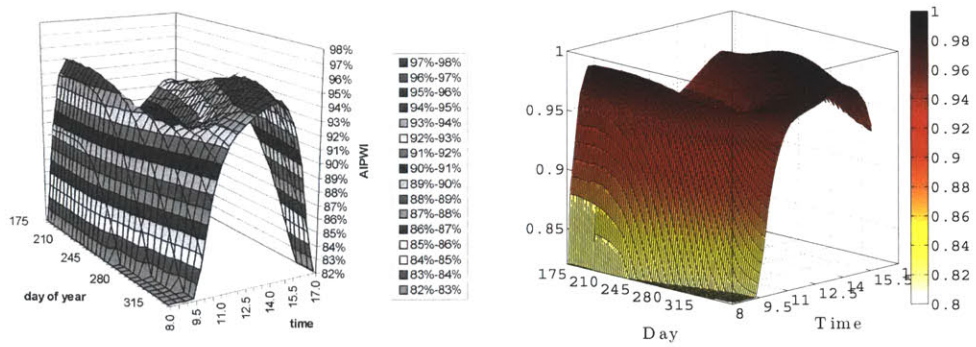

(a) Buck and Teufel, 2009 [6] (b) In-house model

Figure 3-1: Receiver average annual insolation-weighted interception efficiency as a function of design day and time of static canting. The model used herein closely matches both qualitative features and quantitative values of literature results [6].

3.4 Heliostat Canting Case Studies

With the methodology presented in Section 3.2, two case studies are considered. The first is a traditional tower system modeled after PS10, the 11MWe power tower plant located in Andalusia, Spain [1, 3]. The receiver aperture is approximately 100m above the heliostat field, which consists of 624 heliostats each approximately 120m^2 in area. The second case study evaluates the potential improvement of off-axis canting for beam-down heliostats on hillsides, e.g., a plant design called the CSPonD concept [21, 30, 14]. This field design involves placing heliostats on a south-facing hillside (if in the Northern Hemisphere) to reflect light down and directly into a ground-level salt pond. In both case studies, two heliostat designs are considered, (i) facets which are canted based on a single design day and time (referred to as static canting), similar to the validation case study based on Buck and Teufel [6], and (ii) facets which are actively controlled throughout the day such that each facet center is always perfectly focusing (referred to as dynamic canting).

3.4.1 Planar Heliostat Field

In the power tower configuration with a planar heliostat field, the heliostat dimensions and receiver height are modeled after PS10; but unlike PS10, heliostat locations in a full 360° around the tower are considered. Figure 3-2(a) shows the percent reduction in spot size, compared to on-axis parabolic canting, due to static canting of a heliostat as a function of position relative to the tower. The most significant improvement is gained to the south of the tower with approximately 5% reduction in the average annual insolation-weighted spot size. If a cavity receiver is considered such that the acceptance angle requires the heliostat field to be north of the tower (e.g., the PS10 receiver), the spot size reduction is only 1-2%.

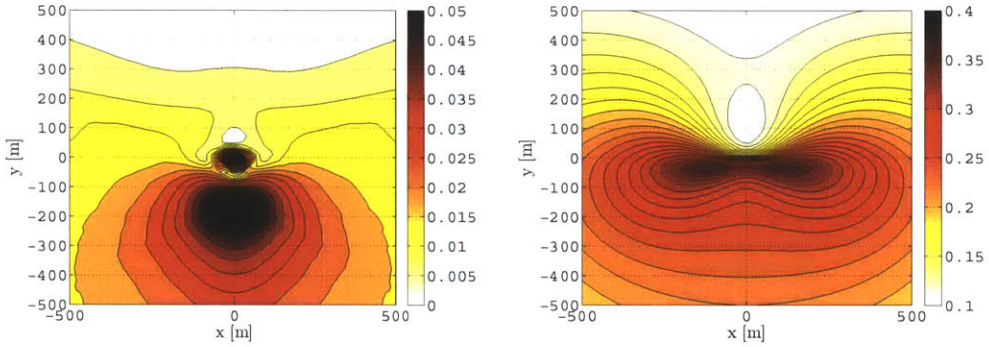

(a) Static canting

(b) Dynamic canting

Figure 3-2: Reduction in average annual insolation-weighted spot size for a planar heliostat field with tower receiver (height = 115m) as a function of field position. The receiver is located at the origin (x=0,y=0).

In the case of dynamic canting, there is a significantly greater opportunity for improvement. Figure 3-2(b) again shows the percent reduction in spot size, yielding an average improvement of 20.8%. The average improvement is calculated as the mean spot size reduction using a uniform distribution of heliostats in the limits of the plot shown. No weighting function was used to reflect the density of an actual heliostat layout nor variations in efficiency. Not only is the spot size reduction more significant in the dynamic case, but the locations with highest improvement are in a west-east line near the receiver, which have a higher cosine efficiency than locations south of the receiver.

3.4.2 Hillside Heliostat Field

The second case study, based on the CSPonD concept [21, 30, 14], utilizes a south-facing hillside as the site for a heliostat field to reflect light downwards. Consequently, and in contrast to a receiver atop a tower, not only are projection (cosine) losses greater but aberration is also greater using on-axis parabolic canting. An idealized hillside is tested in which the ground-level receiver is located 100m south of the base and the hillside is defined by a constant slope in the x-direction (east-west). In both static and dynamic canting, three hillside slopes are considered.

The first scenario, static canting, is presented in Figure 3-3. Similar to the tower configuration presented in Section 3.4.1, the reduction in spot size compared to parabolic canting is small. While the reduction is as much as 5% at locations very close to the receiver, average improvements are again in the 1-2% range. Locations south of the receiver were not considered in this case study because the cosine efficiency of a heliostat focusing light directly into the salt pond from the south, at the same elevation, would be prohibitively low.

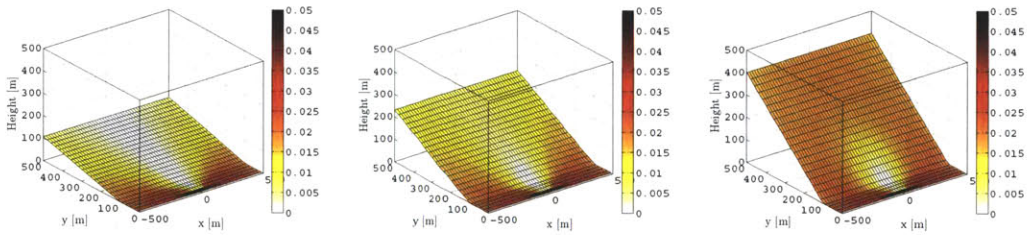

(a) 15° slope, 1.18% average reduction in spot size

(b) 30° slope, 1.41% average reduction in spot size

(c) 45° slope, 1.96% average reduction in spot size

Figure 3-3: Reduction in average annual insolation-weighted spot size for a beam-down hillside heliostat field with static canting as a function of heliostat field position.

The second scenario, dynamic canting, is shown in Figure 3-4 to have potential benefits much greater than the static case, with average improvements ranging from 22.1% to 25% depending on hillside slope. Note that reducing the effective diameter of the receiver by approximately 23% can result in significant improvement in receiver efficiency and motivates dynamic canting instead of on-axis parabolic canting.

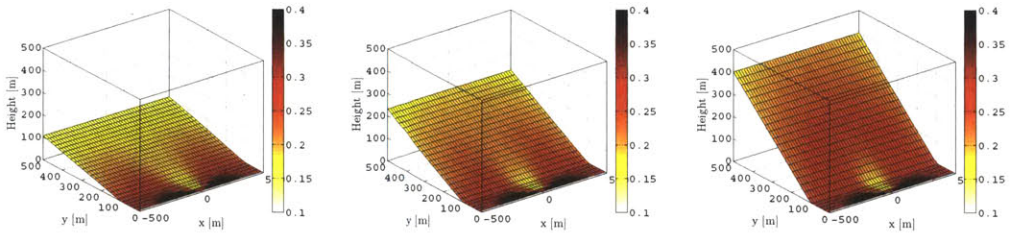

(a) 15° Slope, 22.1% Average Reduction in Spot Size

(b) 30° Slope, 23.4% Average Reduction in Spot Size

(c) 15° Slope, 25.0% Average Reduction in Spot Size

Figure 3-4: Reduction in average annual insolation-weighted spot size for a beam-down hillside heliostat field with dynamic canting as a function of heliostat field position.

3.5 Conclusion

In this article, two off-axis heliostat canting methods are compared to the traditional on-axis parabolic canting. As a metric for comparison, average annual insolation-weighted spot size was minimized. A small spot size allows for uniformly distributing power on the receiver and minimizes losses to the environment, e.g., interception losses or thermal (convective and radiative) losses from the receiver. Both static (i.e., facets rigidly attached to the common frame) and dynamic canting are considered. While the degree of complexity in the heliostat design varies significantly between the two, dynamic canting provides an upper bound on the expected improvement for the case studies considered.

In both planar and hillside heliostat fields, static off-axis canting provided only a small improvement over on-axis canting with roughly a 1-2% reduction in average annual insolation-weighted spot size. In other words, for the same interception efficiency, the receiver effective diameter could be reduced by about 1-2%. In contrast, dynamic canting yielded a more dramatic result, reducing the average spot size by 20-25% in the case studies considered. Whether either canting method is implemented depends on the thermo-economic trade-off of reduced receiver size versus increased heliostat cost. This trade-off has not be considered herein.

Intuitively, beam-down heliostats (located on a hillside) are expected to be significantly better candidates for off-axis canting than heliostats with a tower receiver.

However, based on the results, the method of canting is a much greater influence on performance than the field configuration. This result is explained by a contribution of other factors affecting spot size other than aberration, including surface errors on the mirror and sun shape. Therefore, the spot size has a much greater dependence on heliostat canting and dimensions than on the configuration of the field.

Finally, while not considered in this analysis, is the potential for optimization of static canting. The implicit assumption in this paper is that the optimal annual canting corresponds with an optimal instantaneous canting, which has not been proven. The model has the capability to do such optimization, but is not considered herein.

Appendix A

Horizontal and Cartesian Coordinate Systems

The transformation from the local (body-fixed) frame (Cartesian coordinates, as in Figure A-1, with origin at the heliostat or aperture center) to the global coordinate system is calculated via the rotation $\left([R]^{-1} = [R]^T\right)$ and translation [31]. The azimuth and altitude (shown in Figure A-1) are defined with respect the surface normal direction.

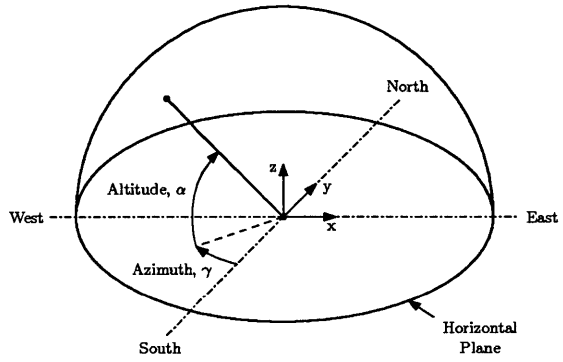

Figure A-1: Horizontal and Cartesian Coordinate Systems

$$
\begin{aligned}
\hat{\mathbf{x}}_{\text{global}} &= [R]\hat{\mathbf{x}}_{\text{local}} + \hat{\mathbf{x}}_{\text{center}} \\
&= \begin{bmatrix} \cos\gamma & \sin\alpha\sin\gamma & -\cos\alpha\sin\gamma \\ -\sin\gamma & \sin\alpha\cos\gamma & -\cos\alpha\cos\gamma \\ 0 & \cos\alpha & \sin\alpha \end{bmatrix} \hat{\mathbf{x}}_{\text{local}} + \hat{\mathbf{x}}_{\text{center}}
\end{aligned}
$$

Bibliography

[1] PS10: a 11.0-MWe Solar Tower Power Plant with Saturated Steam Receiver. presentation, Comillas University. http://www.upcomillas.es/catedras/crm/report05/Comunicaciones/Mesa%20IV/D.%20Valerio%20Fern%C3%A1ndez%20-%20Solucar%202.pdf [Last accessed: April 2011].

[2] National Solar Radiation Data Base. Technical report, National Renewable Energy Laboratory, 1617 Cole Blvd., Golden, Colorado 80401, September 1992.

[3] 10MW Solar Thermal Power Plant for Southern Spain: Final Technical Progress Report. Technical report, Sunlúcar, 2005. http://ec.europa.eu/energy/res/sectors/doc/csp/ps10_final_report.pdf [Last accessed: April 2011].

[4] V. Badescu, editor. *Modeling Solar Radiation at the Earth's Surface: Recent Advances.* Springer, 2008.

[5] B. Belhomme, R. Pitz-Paal, P. Schwarzboezl, and S. Ulmer. A New Fast Ray Tracing Tool for High-Precision Simulation of Heliostat Fields. *Journal of Solar Energy Engineering-Transactions of the ASME*, 131(3), August 2009.

[6] R. Buck and E. Teufel. Comparison and Optimization of Heliostat Canting Methods. *Journal of Solar Energy Engineering-Transactions of the ASME*, 131(1), February 2009.

[7] F. J. Collado. Quick Evaluation of the Annual Heliostat Field Efficiency. *Solar Energy*, 82(4):379–384, 2008.

[8] F. J. Collado and J. A. Turegano. Calculation of the Annual Thermal-Energy Supplied by a Defined Heliostat Field. *Solar Energy*, 42(2):149–165, 1989.

[9] ESRI Data and Maps [GIS software] [CD-ROM]. Arcmap v9.3, 2008.

[10] J. A. Duffie and W. A. Beckman. *Solar Engineering of Thermal Processes.* Wiley, 2006.

[11] R. Eden, M. Posner, R. Bending, E. Crouch, and J. Stanislaw. *Energy Economics: Growth, Resources, and Policies.* Cambridge University Press, New York, 1981.

[12] M. Elsayed, M. Habeebuallah, and O. Alrabghi. Yearly-Averaged Daily Usefulness Efficiency of Heliostat Surfaces. *Solar Energy*, 49(2):111–121, Aug 1992.

[13] P. Garcia, A. Ferriere, and J.-J. Bezian. Codes for Solar Flux Calculation Dedicated to Central Receiver System Applications: A Comparative Review. *Solar Energy*, 82(3):189–197, 2008.

[14] A. Ghobeity, C. J. Noone, C. N. Papanicolas, and A. Mitsos. Optimal time-invariant operation of a power and water cogeneration solar-thermal plant. *In Press: Solar Energy*, June 20, 2011. http://dx.doi.org/10.1016/j.solener.2011.06.023.

[15] Google. Google Earth Pro. `http://earth.google.com/`, 2010.

[16] A. Griewank and A. Walther. *Evaluating Derivatives: Principles and Techniques of Algorithmic Differentiation, Second Edition.* Society for Industrial and Applied Mathematic, 2008.

[17] L. Hascoët and V. Pascual. TAPENADE 2.1 user's guide, September 2004.

[18] H. Hottel. A Simple Model for Estimating Transmittance of Direct Solar-Radiation Through Clear Atmospheres. *Solar Energy*, 18(2):129–134, 1976.

[19] R. V. Jean. *Phyllotaxis: A Systemic Study in Plant Morphogenesis.* Cambridge Studies in Mathematics. 1994.

[20] B. L. Kistler. A User's Manual for DELSOL3: A Computer Code for Calculating the Optical Performance and Optimal System Design for Solar Thermal Central Receiver Plants. Technical report, November 1986.

[21] C. J. Noone, A. Ghobeity, A. H. Slocum, G. Tzamtzis, and A. Mitsos. Site Selection for Hillside Central Receiver Solar Thermal Plants. *Solar Energy*, 85(5):839–848, May 2011.

[22] C. J. Noone, M. Torrilhon, and A. Mitsos. Heliostat field optimization: A new computationally efficient model and biomimetic layout. Sumbitted for Publication.

[23] A. Rabl. *Active Solar Collectors and Their Applications.* Oxford University Press, USA, 1985.

[24] I. Reda and A. Andreas. Solar Position Algorithm for Solar Radiation Applications. Technical report, January 2008. NREL Report No. TP-560-34302.

[25] J. N. Ridley. Packing efficiency in sunflower heads. *Mathematical Biosciences*, 58(1):129–139, 1982.

[26] E. Rodriguez, C. S. Morris, J. E. Belz, E. C. Chapin, J. M. Martin, W. Daffer, and S. Hensley. An Assessment of the SRTM Topographic Products. Technical Report JPL D-31639, Jet Propulsion Laboratory, Pasadena, California, 2005.

[27] M. Schmitz, P. Schwarzbozl, R. Buck, and R. Pitz-Paal. Assessment of the Potential Improvement Due to Multiple Apertures in Central Receiver Systems with Secondary Concentrators. *Solar Energy*, 80(1):111–120, 2006.

[28] A. H. Slocum. Concepts for Robust Renewable Energy Generation and Storage. `http://alum.mit.edu/sites/default/files/migrated/learn/docs/SlocumEnergyResearchTalk11.16.2009.pdf`. accessed 4 August 2010.

[29] A. H. Slocum, J. Buongiorno, C. W. Forsberg, D. S. Codd, and A. T. Paxson. Concentrated Solar Power System. PCT Patent Application PCT/US10/49474, 18 Sep 2009.

[30] A. H. Slocum, D. S. Codd, J. Buongiorno, C. Forsberg, T. McKrell, J.-C. Nave, C. N. Papanicolas, A. Ghobeity, C. J. Noone, S. Passerini, F. Rojas, and A. Mitsos. Concentrated Solar Power on Demand. *Solar Energy*, 85(7):1519–1529, July 2011.

[31] S. T. Thornton and J. B. Marion. *Classical Dynamics of Particles and Systems.* Brooks Cole, 2003.

[32] United States Geological Survey (USGS). Shuttle Radar Topography Mission (SRTM). `http://www2.jpl.nasa.gov/srtm/`. 1 Arc Second Data, Version 2.1.

[33] H. Vogel. Better Way to Construct the Sunflower Head. *Mathematical Biosciences*, 44(3-4):179–182, 1979.

[34] X. Wei, Z. Lu, Z. Wang, W. Yu, H. Zhang, and Z. Yao. A New Method for the Design of the Heliostat Field Layout for Solar Tower Power Plant. *Renewable Energy*, 35(9):1970–1975, September 2010.

[35] T. Wendelin. SolTRACE: A New Optical Modeling Tool for Concentrating Solar Optics. National Renewable Energy Laboratory (NREL), International Solar Energy Conference, March 2003.

[36] Z. Yao, Z. Wang, Z. Lu, and X. Wei. Modeling and Simulation of the Pioneer 1 MW Solar Thermal Central Receiver System in China. *Renewable Energy*, 34(11):2437–2446, Nov 2009.

[37] A. Yogev, A. Kribus, M. Epstein, and A. Kogan. Solar "Tower Reflector" Systems: A New Approach for High-Temperature Solar Plants. *International Journal Hydrogen Energy*, 23(4):239–245, 1998.